ARTICLE

BIOTECHNOLOGY and BIOENGINEERING

A Model of Fluid–Biofilm Interaction Using a Burger Material Law

Brett W. Towler,[1] Al Cunningham,[2] Paul Stoodley,[3] Ladean McKittrick[1]

[1]Civil Engineering Department, Montana State University, 205 Cobleigh Hall, Bozeman, Montana 59717-3900; telephone: 406-994-1566; fax: 406-994-6105; e-mail: BrettT@ce.montana.edu

[2]Center for Biofilm Engineering, Montana State University, Bozeman, Montana

[3]Center for Genomic Sciences, Allegheny-Singer Res. Institute, Pittsburgh, Penn

Received 25 January 2006; accepted 19 June 2006

Published online 24 July 2006 in Wiley InterScience (www.interscience.wiley.com). DOI 10.1002/bit.21098

ABSTRACT: A two-dimensional finite element model of the biofilm response to flow was developed. The numerical code sequentially coupled the fluid dynamics of turbulent, incompressible flow with the mechanical response of a single hemispherical biofilm cluster (~100 μm) attached to the flow boundary. A non-linear Burger material law was used to represent the viscoelastic response of a representative microbial biofilm. This constitutive law was incorporated into the numerical model as a Prony series representation of the biofilm's relaxation modulus. Model simulations illuminated interesting details of this fluid–structure interaction. Simulations revealed that softer biofilms (characterized by lower elastic moduli) were highly susceptible to lift forces and consequently were subject to even greater drag forces found higher in the velocity field. A bimodal deformation path due to the two Burger relaxation times was also observed in several simulations. This suggested that interfacial biofilm may be most susceptible to hydrodynamically induced detachment during the initial relaxation time. This result may prove useful in developing removal strategies. Additionally, plots of lift versus drag suggested that the deformation paths taken by viscoelastic biofilms are largely insensitive to specific material coefficients. Softer biofilms merely seem to follow the same path (as a stiffer biofilm) at a faster rate. These relationships may be useful in estimating the hydrodynamic forces acting on an attached biofilm based on changes in scale and cataloged material properties.

Biotechnol. Bioeng. 2007;96: 259–271.

KEYWORDS: biofilm; viscoelastic; biofouling; hydraulic; burger; mechanics

Introduction

Bacterial aggregations and their activities on wetted interfaces are collectively referred to as 'biofilms.' The pervasiveness of this microbial activity and its associated economic impacts are of major concern to hydraulic engineers and environmental professionals alike (Characklis, 1990). Biofilm accumulation on water mains contributes to the contamination of drinking water due to continuous microbial growth and hydrodynamically induced detachment processes (Geesey and Bryers, 2000). Interfacial biofilm growth has also been shown to significantly affect the performance of piping systems (Zelver, 1979). Indeed, given the ubiquity of this microbial activity, biofilm may be the single most underrepresented hydrodynamic boundary condition.

Despite the prevalence of biofilms in man-made systems, a fundamentally sound description of biofilm–fluid interaction does not exist. From an engineering standpoint, understanding the material properties of biofilm is a necessary first step toward the development of such a description. Unfortunately, issues related to complex boundary conditions and turbulent closure of the governing equations preclude a general analytical solution. Computational methods are frequently used as a complimentary approach.

To that end, a computer model of the biofilm response to flow was developed by incorporating a Burger material model using experimentally derived biofilm viscoelastic parameters with a computational fluids dynamics code. This program employs the finite element method to model the response of a single attached biofilm cluster to a turbulent flow field. The structural response of the cluster is represented with a viscoelastic material law. The Navier–Stokes equations are used to describe the hydrodynamics of the flow. The mechanics of the biofilm cluster and bulk fluid are sequentially coupled. Model simulations have illuminated interesting details of this interaction.

Correspondence to: B.W. Towler

Material Science of Biofilms

While the composition of biofilm can include any number of organic and non-organic materials, the physical properties of biofilm are largely dependent upon the specific microbial species and its form of extra-cellular polymeric slime (EPS). In general, polymers are chains of organic molecules and a solvent (Shackelford, 1985). Cross-linking occurs when adjacent chains are chemically bonded. This bonding acts to resist vibration and rotation of the chains, thereby lending strength to the polymer (Callister, 1985). Biofilm is often regarded as a biosynthetic polymer (Flemming et al., 2002).

Structure and Rheology

Many investigators have identified different transient forms and structural features in biofilms including clusters, ripples, dunes, and finger-like projections called 'streamers' (Dockery and Klapper, 2001; Gjaltema et al., 1994; Stoodley et al., 1997,). The relationship between these structures and bulk fluid hydrodynamics has been studied. Stoodley et al. (1999a) grew mixed culture biofilms consisting of *Klebsiella pneumoniae*, *Pseudomonas aeruginosa*, *Pseudomonas fluorescens*, and *Stenotrophomonas maltophilia* in glass flow cells under different hydrodynamic conditions. Short-term changes in mean velocity resulted in migration and elongation of the biofilm structures. The flow cell work illustrated the interplay between biofilm rheology and local flow field. However, Stoodley's study was essentially a study of biofilm kinematics; fluid forces and biofilm material properties were not accounted for.

Biofilm Mechanics

Biofilms respond to stresses induced by a flowing fluid. The nature of that response is greatly influenced by intrinsic material properties. Nevertheless, many models do not account for these properties (Dockery and Klapper, 2001; Gujer and Wanner, 1990; Hermanowicz, 1998). Those that have recognized the relevance of material properties are often limited in applicability (Picioreanu et al., 2001).

Stoodley et al. (1999b, 2002) developed an experimental technique for testing biofilms response to turbulent flow conditions. Microbial biofilms were grown in glass flow-through reactors and using digital time lapse microscopy, measurements of elongation versus changes in flow rate were taken. While the methods developed for these studies were highly novel and the results equally informative, neither the applied loads nor deformations were actually measured. Instead, wall shear stress was used in lieu of the actual hydrodynamic load. The angular deformation of a streamer's leading edge was used as an approximation of the true shear strain. Applied fluid loads are complex, multi-directional forces and are poorly approximated by a constant, unidirectional wall shear force. Indeed, by assuming a constant wall shear stress one completely neglects the interplay between biofilm structure and local hydrodynamics. Furthermore, the deformation exhibited by the streamers was equally complex. Finally, the shear-stress relation was improperly couched in a form of Hooke's Law; a viscoelastic response was clearly indicated. Therefore, the transferability of the calculated elastic moduli and shear coefficients presented in these studies is limited.

Picioreanu et al. (2001) developed a two-dimensional model of biofilm detachment that includes an elastic response to fluid stress. While the geometry of this multi-dimensional model is more realistic, the elastic constitutive relation does not agree with the viscoelastic responses observed by other investigators (Ohashi and Harada, 1994).

The deformational response of any material (e.g., biofilm) to stress is specified by a so-called 'constitutive law.' The development of a constitutive law is a complex process because a material's strain response may vary with, among other things, temperature, strain rate, and the magnitude of applied loads (Mase and Mase, 1999). Towler et al. (2003), used a conventional material testing approach by performing creep tests on mixed population biofilms in a rotating disk rheometer. These results provided further confirmation of a non-linear material law and suggested the applicability of a linear viscoelastic Burger model. The Burger model is a serial combination of the Maxwell and Kelvin spring-dashpot analogs (Findley et al., 1989). The one-dimensional differential equation for this four parameter viscoelastic model takes the form

$$\sigma + \left(\frac{\eta_1}{E_1} + \frac{\eta_1}{E_2} + \frac{\eta_2}{E_2}\right)\frac{\partial \sigma}{\partial t} + \left(\frac{\eta_1 \eta_2}{E_1 E_2}\right)\frac{\partial^2 \sigma}{\partial t^2} = \eta_1 \frac{\partial \varepsilon}{\partial t} + \left(\frac{\eta_1 \eta_2}{E_2}\right)\frac{\partial^2 \varepsilon}{\partial t^2} \quad (1)$$

where σ is the axial (or shear) stress loading, ε is the axial (or shear) strain response, t is the independent time variable, η_1 and η_2 are the 1st and 2nd viscous coefficients, respectively, and E_1 and E_2 are the 1st and 2nd elastic coefficients, respectively.

Hydrodynamic Impact

The hydrodynamic impact of biofilm accumulation is well documented (Bryers and Characklis, 1981). In general, hydrodynamic resistance is a function of both surface drag and form drag (Currie, 1974; Rouse, 1946). Surface drag is due to the frictional resistance of a fluid boundary. Form drag is an expression of pressure differentials due to boundary layer separation. In the context of biofouling, this suggests there are two causes of hydrodynamic drag: biofilm 'skin' friction and form drag due to the geometry of the biofilm structures (e.g., ripples, dunes, streamers). It has been posited that the viscoelastic nature of biofilm is the cause of documented pressure drops in pipelines (Picologlou et al., 1980). This would imply that frictional

DOI 10.1002/bit

resistance is time dependant. Several investigators have posited that pressure drop due to increased frictional resistance occurs when biofilm growth exceeds the thickness of the laminar sublayer (Characklis, 1979; McCoy and Costerton, 1982). Since uniform biofilm accumulation would effectively redefine the viscous sublayer, these conclusions imply that form drag is the operative cause of biofilm-induced pressure drop. This implication was supported by Stoodley et al. (1998).

Biofilm shape, structure, and material response are manifestly linked to the hydrodynamics of pipelines and other devices subject to biofouling. Thus, the economic and engineering-related impacts, previously alluded to, serve as catalysts for examining the biofilm stress-strain relation in detail. A coupled computational model was used to elucidate the interaction of biofilm structure shape, material law, and near surface fluid dynamics.

Materials and Methods

A computational simulation of the interaction between a biofilm structure and the bulk fluid would alleviate the need to repeatedly measure velocities and deformations directly and act as a tool for further investigation of the biofilm response to turbulent flow. For comparison, the approximate scale, geometry, and flow regime of the experiments performed by Stoodley et al. (1999b) were duplicated in the simulations described below.

Model Description

A 100 μm radius compliant half circle representing an attached biofilm structure was anchored at the low y side to a channel that was 3 mm in height (Fig. 1). The biofilm cluster was modeled as a half circle in a two dimensional structural domain. In three dimensions, a hemispherical shape is analogous to an idealized growth pattern for a microbial community in the absence of a strong unidirectional flow field. Thus, this hemispherical shape could be regarded as the starting point of biofilm deformation. This elementary shape was chosen in hopes of elucidating behavior that more complex geometries might mask.

The bulk fluid domain was bounded by a 40 mm long by 3146 mm high two-dimension channel approximating the 200 mm long, 3 mm wide square glass flow tube used by Stoodley et al. (1999b). The simulated channel was 40 mm in length with the biofilm structure placed at the center. Thus, the model allowed for a 20 mm entrance length and a 20 mm exit length. This distance was chosen as a compromise between the computational demands of modeling the entire length and the length necessary to prevent entrance and exit effects. Initial testing indicated that the 20 mm exit length was sufficient to prevent any "back flushing" effects due to the presence of a prescribed pressure at the downstream boundary. However, it was also revealed that the flow field (i.e., velocity distribution) was not yet fully developed as it approached the biofilm structure. To mitigate the need for an extended entrance length, a non-uniform velocity distribution was applied at the inlet boundary.

Boundary Conditions

The velocity distribution in turbulent flows is not constant yet considerably more uniform than the parabolic distribution observed in laminar flows. While the velocity distribution in laminar flow can be determined analytically (Janna, 1993), this is not possible under turbulent conditions. However, a number of empirical formulae exist. For smooth pipes, Giles et al. (1956) suggests

$$v(y) = V\sqrt{f}\left(2\log\frac{y}{R} + 1.32\right) + V \qquad (2)$$

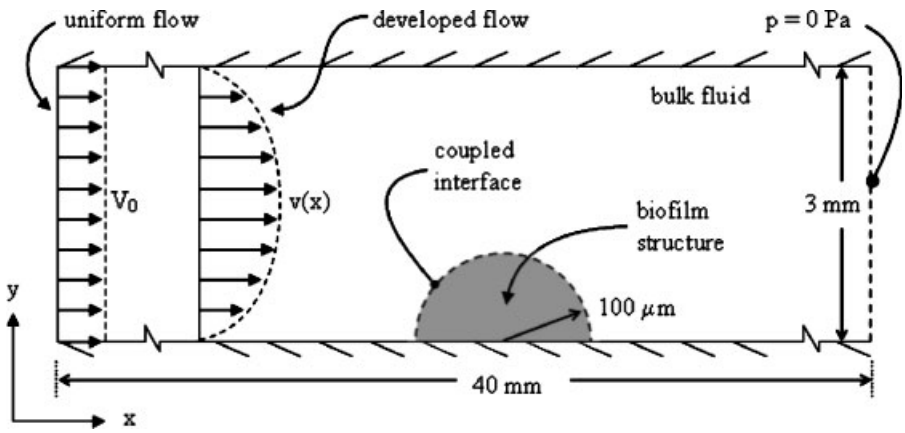

Figure 1. Biofilm Model Description: Water moves from left to right impinging on the attached viscoelastic biofilm hemisphere.

where $v(y)$ is the velocity at a distance y from the center of the conduit, R is the radius of the conduit, V is the mean velocity, and f is the friction factor. This Equation (2) requires an estimate of the friction factor. For smooth pipes, the Blasius equation can be used to approximate the friction factor (Debler, 1990),

$$f = \frac{0.316}{RE^{0.25}} \tag{3}$$

where RE is the dimensionless pipe Reynolds Number. Using custom code written in FORTRAN, these two equations were combined to specify velocities at the nodes on the inlet boundary. Water ($\mu = 1.0 \times 10^{-6}$ kg/mm · s, $\rho = 1.0 \times 10^{-6}$ kg/mm^3) moved from the left to right at a mean velocity of 1.0 m/s, matching the experimental set-up of Stoodley et al. (1999b). Water, flowing in the positive x direction, entered through an inlet at the low x boundary and exited the channel through an outlet at the high x boundary.

In addition to the inlet boundary condition, the so-called "no slip" condition was applied to the channel walls and the biofilm/fluid interface. The flow boundaries were prescribed as hydraulically smooth. The walls were also fixed in space; the biofilm/fluid interface was not. Thus, momentum transfer between the moving water and the cluster surface was allowed to deform the biofilm shape. Finally, a uniform pressure boundary was prescribed at the channel outlet.

Constitutive Equation

Previous studies have shown that laboratory-grown biofilm demonstrates a viscoelastic response to stress (Klapper et al., 2002; Korstgens et al., 2001; Stoodley et al., 1999b). Moreover, these studies suggested that biofilms behave like viscoelastic fluids (i.e., materials that exhibit continuous strain under a constant load). Based on previous experimental work (Towler et al., 2003), a linear viscoelastic Burger model was used as a constitutive law for microbial biofilm. Integration of the Burger differential Equation (1) leads to the general strain equation

$$\begin{aligned}\varepsilon_{ij}(t) = \delta_{ij}\Bigg[\left(\frac{1}{R_1} - \frac{1}{G_1}\right)\sigma_{kk}(t) + \int_0^t \Bigg[-\frac{1}{G_2}(1 - e^{-G_2(t-\xi)/\eta_2}) \\ - \frac{(t-\xi)}{\eta_1}\Bigg]\frac{\partial \sigma_{kk}(\xi)}{\partial \xi}\,\mathrm{d}\xi\Bigg] + \frac{1}{G_1}\sigma_{ij}(t) \\ + \int_0^t \left[\frac{1}{G_2}(1 - \mathrm{e}^{-G_2(t-\xi)/\eta_2}) + \frac{(t-\xi)}{\eta_1}\right]\frac{\partial \sigma_{ijk}(\xi)}{\partial \xi}\,d\xi\end{aligned} \tag{4}$$

where ε_{ij} is the strain on the e_j plane in the e_i direction, δ is the Kroneker delta, σ_{ij} is the stress tensor, t is the time variable, R_1 is the bulk elastic modulus, G_1 and η_1 are the shear modulus and viscous coefficient, respectively, for the Maxwell component of the Burger model, and G_2 and η_2 are the shear modulus and viscous coefficient, respectively, for the Kelvin component. The Maxwell component refers to a standard linear viscoelastic fluid developed from spring and dashpot analogs in series. Similarly, the Kelvin component refers to a standard linear viscoelastic solid developed from spring and dashpot analogs in parallel. The Burger model's analog is a Kelvin analog in series with a Maxwell analog. This Equation (4) describes the strain response as a function of stress for an isotropic mixed culture biofilm.

The relaxation modulus of any linear viscoelastic material can be represented as the stress per unit of applied strain. Conveniently, the Burger model can used in ANSYS by converting the relaxation modulus of Equation (4) into a Prony series of the form

$$C(t) = C_0 + \sum_{i=1}^{k} C_i \mathrm{e}^{-a_i t} \tag{5}$$

where $C(t)$ is the dependent variable, t is the independent variable, i is a dummy index, $k+1$ defines the number of terms in the series, and C_i and a_i are scalar coefficients. The relaxation modulus is a normalized representation of a materials ability to dissipate internal stresses under a constant strain. The relaxation modulus, $G(t)$, was determined through a Laplace transform of the creep compliance.

$$\begin{aligned}G(t) = &\frac{\left(\eta_1 - \frac{\eta_1\eta_2}{G_2}T_1\right)}{\sqrt{\left(\frac{\eta_1}{G_1} + \frac{\eta_1}{G_2} + \frac{\eta_2}{G_2}\right)^2 - 4\frac{\eta_1\eta_2}{G_1G_2}}}\mathrm{e}^{-T_1 t} \\ &+ \frac{-(\eta_1 - \frac{\eta_1\eta_2}{G_2}T_2)}{\sqrt{\left(\frac{\eta_1}{G_1} + \frac{\eta_1}{G_2} + \frac{\eta_2}{G_2}\right)^2 - 4\frac{\eta_1\eta_2}{G_1G_2}}}\mathrm{e}^{-T_2 t}\end{aligned} \tag{6}$$

where η_1 is the viscosity coefficient in the Maxwell element, G_1 is the (elastic) shear coefficient in the Maxwell element, η_2 is the viscosity coefficient in the Kelvin element, G_2 is the shear coefficient in the Kelvin element, and T_1 and T_2 are defined as

$$T_1 = \frac{\frac{\eta_1}{G_1} + \frac{\eta_1}{G_2} + \frac{\eta_2}{G_2} - \sqrt{\left(\frac{\eta_1}{G_1} + \frac{\eta_1}{G_2} + \frac{\eta_2}{G_2}\right)^2 - 4\frac{\eta_1\eta_2}{G_1G_2}}}{2\frac{\eta_1\eta_2}{G_1G_2}} \tag{7}$$

and

$$T_2 = \frac{\frac{\eta_1}{G_1} + \frac{\eta_1}{G_2} + \frac{\eta_2}{G_2} + \sqrt{\left(\frac{\eta_1}{G_1} + \frac{\eta_1}{G_2} + \frac{\eta_2}{G_2}\right)^2 - 4\frac{\eta_1\eta_2}{G_1G_2}}}{2\frac{\eta_1\eta_2}{G_1G_2}} \tag{8}$$

DOI 10.1002/bit

By equating Equation (4) with Equation (5), the following linear and exponential Prony coefficients can be explicitly represented in terms of Burger model spring and dashpot parameters:

$$C_1 = \frac{\left[\eta_1 - \frac{\eta_1\eta_2}{G_2}\left(\frac{\frac{\eta_1}{G_1}+\frac{\eta_1}{G_2}+\frac{\eta_2}{G_2}-\sqrt{\left(\frac{\eta_1}{G_1}+\frac{\eta_1}{G_2}+\frac{\eta_2}{G_2}\right)^2-4\frac{\eta_1\eta_2}{G_1G_2}}}{2\frac{\eta_1\eta_2}{G_1G_2}}\right)\right]}{\sqrt{\left(\frac{\eta_1}{G_1}+\frac{\eta_1}{G_2}+\frac{\eta_2}{G_2}\right)^2-4\frac{\eta_1\eta_2}{G_1G_2}}} \quad (9)$$

$$C_2 = \frac{-\left[\eta_1 - \frac{\eta_1\eta_2}{G_2}\left(\frac{\frac{\eta_1}{G_1}+\frac{\eta_1}{G_2}+\frac{\eta_2}{G_2}+\sqrt{\left(\frac{\eta_1}{G_1}+\frac{\eta_1}{G_2}+\frac{\eta_2}{G_2}\right)^2-4\frac{\eta_1\eta_2}{G_1G_2}}}{2\frac{\eta_1\eta_2}{G_1G_2}}\right)\right]}{\sqrt{\left(\frac{\eta_1}{G_1}+\frac{\eta_1}{G_2}+\frac{\eta_2}{G_2}\right)^2-4\frac{\eta_1\eta_2}{G_1G_2}}} \quad (10)$$

$$a_1 = \frac{\frac{\eta_1}{G_1}+\frac{\eta_1}{G_2}+\frac{\eta_2}{G_2}-\sqrt{\left(\frac{\eta_1}{G_1}+\frac{\eta_1}{G_2}+\frac{\eta_2}{G_2}\right)^2-4\frac{\eta_1\eta_2}{G_1G_2}}}{2\frac{\eta_1\eta_2}{G_1G_2}} \quad (11)$$

$$a_2 = \frac{\frac{\eta_1}{G_1}+\frac{\eta_1}{G_2}+\frac{\eta_2}{G_2}+\sqrt{\left(\frac{\eta_1}{G_1}+\frac{\eta_1}{G_2}+\frac{\eta_2}{G_2}\right)^2-4\frac{\eta_1\eta_2}{G_1G_2}}}{2\frac{\eta_1\eta_2}{G_1G_2}} \quad (12)$$

Finite Element Solver

ANSYS version 7.1, a commercially available finite element code, was used to solve the fundamental equations of motion, equations of state, and constitutive laws for both the fluid and structural domains in two spatial dimensions. The fluid mesh was created using four node two dimensional plane elements. The biofilm mesh was created using eight node two dimensional plane elements. The fluid processor iteratively solved the linearized governing partial differential equations using a method based on the SIMPLE technique developed by Patankar (1980). The software employs the principle of virtual work (ANSYS, 2003) to develop the partial differential equations representing the structural response (i.e., biofilm behavior). A recursive sequential algorithm was then used to couple the two phases (i.e., bulk fluid, biofilm cluster) across one a dimensional, dissimilarly meshed interface.

The machine used was a Silicon Graphics, Inc., SGI Origin 2100. The Origin 2100 has eight 350 MHz processors and 4 gigabytes of RAM. The time to solution for simulations was approximately 6 h. The convergence criterion used by the FSI algorithm was the Euclidean norm, l_2, of the forces and displacements transferred across the interface. The time-marching method of the solution can be regarded as quasi-static. That is, at each time step a 'solution' is reached. A 'converged' solution for each time step is one where the differences between these Euclidean norms approaches zero.

Parametric Studies

Several ANSYS simulations were generated to investigate how a viscoelastic biofilm cluster might respond to changes in material properties, cluster size, and bulk hydrodynamics. A 'series-set' nomenclature was used in this parametric study. A 'series' represents a collection of simulations (or 'sets') in which a single parameter is varied from a common baseline set (set 5 in all series). Nine series were created (named A through I); there were a maximum of nine sets within each series, numbered one through nine. Thus, each set represents an ANSYS simulation using a different value of the parameter being varied in its parent series. Parameter values were decreased in sets 4 through 1. Parameter values were increased in sets 5 through 9. For example, the shear modulus G_1 is varied in series A and the specific set A4 represents a decrease in G1 from the baseline set A5. The baseline sets (A5, B5, . . . , F5) are identical in order to preserve consistency across all series. The parameters in the baseline set were chosen such that the biofilm strain response was approximately equal to the strain observed by Stoodley et al. (1999b). Table I lists the permutations, by series and set, used in this parametric study.

In series A–D the values of the four viscoelastic material parameters were varied. The value of the Maxwell element shear modulus, G_1, was varied in series A; the relaxation time for the Maxwell element, τ_1, was held constant. Note, τ_1, the Maxwell relaxation time, is simply the ratio of η_1 to G_1. Accordingly, the Maxwell viscous coefficient, η_1, changed in response to G_1. In the next series (B), the value of the Kelvin element shear modulus, G_2, was varied; the relaxation time for the Kelvin element, τ_2, was held constant. The Kelvin viscous coefficient, η_2, changed in response to G_2. In series C, the value of the Maxwell element shear modulus, G_1, was varied again. However, in contrast to Series A, the viscous coefficient, η_1, was held constant. Consequently, the Maxwell relaxation time, τ_1, changed in response to G_1. In the fourth series (D), the value of the Kelvin element shear modulus, G_2, was varied again. In contrast to Series B, the viscous coefficient, η_2, was held constant. Consequently, the Kelvin relaxation time, τ_2, changed in response to G_2.

In series E and F, the magnitude of the mean stream velocity was altered. In series G and H, the effective surface area of the attached biofilm was altered by changing the radius of the biofilm hemisphere. In Series G, the radius was decreased from 0.20 to 0.15 mm. In Series H the radius was increased from 0.20 to 0.25 mm. Series I consisted of a single simulation of Set I5. In this scenario, the biofilm was modeled as a purely elastic material with a Young's modulus of 10 kg/mm·s^2. This value matched the magnitude

Table I. Parametric permutations.

#	Set	G_1 (kg/mm-s^2)	η_1 (kg/mm-s)	τ_1 (s)	G_2 (kg/mm-s^2)	η_2 (kg/mm-s)	τ_2 (s)	V (m/s)	r (mm)
1	A1	1.77	26.5	15	20	100	5	1	0.2
2	A2	2.22	33.3	15	20	100	5	1	0.2
3	A3	3.00	45.0	15	20	100	5	1	0.2
4	A4	4.62	69.2	15	20	100	5	1	0.2
5	A5	10	150	15	20	100	5	1	0.2
6	A6	13.04	195.6	15	20	100	5	1	0.2
7	A7	18.74	281.2	15	20	100	5	1	0.2
8	A8	33.31	499.6	15	20	100	5	1	0.2
9	A9	149.26	2238.9	15	20	100	5	1	0.2
10	B1	10	150	15	0.688	3.441	5	1	0.2
11	B2	10	150	15	0.907	4.536	5	1	0.2
12	B3	10	150	15	1.331	6.653	5	1	0.2
13	B4	10	150	15	2.495	12.477	5	1	0.2
14	B5	10	150	15	20	100	5	1	0.2
15	B6	10	150	15	24.253	121.267	5	1	0.2
16	B7	10	150	15	30.805	154.024	5	1	0.2
17	B8	10	150	15	42.205	211.024	5	1	0.2
18	B9	10	150	15	67.132	267.323	5	1	0.2
19	C1	0.667	150	224.926	20	100	5	1	0.2
20	C2	0.870	150	172.444	20	100	5	1	0.2
21	C3	1.250	150	119.963	20	100	5	1	0.2
22	C4	2.223	150	67.481	20	100	5	1	0.2
23	C5	10	150	15	20	100	5	1	0.2
24	C6	12.120	150	12.376	20	100	5	1	0.2
25	C7	15.382	150	9.752	20	100	5	1	0.2
26	C8	21.044	150	7.128	20	100	5	1	0.2
27	C9	33.306	150	4.504	20	100	5	1	0.2
28	D1	10	150	15	0.983	100	101.704	1	0.2
29	D2	10	150	15	2.636	100	37.932	1	0.2
30	D3	10	150	15	5.030	100	19.879	1	0.2
31	D4	10	150	15	9.140	100	10.941	1	0.2
32	D5	10	150	15	20	100	5	1	0.2
33	D6	10	150	15	24.297	100	4.116	1	0.2
34	D7	10	150	15	30.878	100	3.239	1	0.2
35	D8	10	150	15	42.310	100	2.364	1	0.2
36	D9	10	150	15	67.168	100	1.489	1	0.2
37	E3	3.001	45.011	15	20	100	5	0.8	0.2
38	E5	10	150	15	20	100	5	0.8	0.2
39	E7	18.744	281.163	15	20	100	5	0.8	0.2
40	F4	4.616	69.244	15	20	100	5	1.2	0.2
41	F5	10	150	15	20	100	5	1.2	0.2
42	F7	18.744	281.163	15	20	100	5	1.2	0.2
43	G3	3.001	45.011	15	20	100	5	1	0.15
44	G5	10	150	15	20	100	5	1	0.15
45	G7	18.744	281.163	15	20	100	5	1	0.15
46	H3	3.001	45.011	15	20	100	5	1	0.25
47	H5	10	150	15	20	100	5	1	0.25
48	H7	18.744	281.163	15	20	100	5	1	0.25

of the Maxwell elastic modulus in the baseline simulation, set 5.

Results

The model successfully converged in all but three simulations. The deformations in A1 and A2 were large enough to compress downstream elements to the point where the element volumes became zero or negative. This resulted in convergence failure. The remaining simulations in series A converged successfully. All simulations in series B, C, and D converged successfully. In Series E, simulations 3, 5, and 7 were run using a channel velocity of 800 mm /s. In Series F, simulations 4, 5, and 7 were run using a channel velocity of 1,200 mm /s. Set F4 was used in lieu of Set F3 which also produced displacement great enough to cause convergence failure.

Resolving Hydrodynamic Load into Drag and Lift Forces

The force a fluid imparts to a boundary can be classified as one of two forms. Pressure forces are those that act normal

DOI 10.1002/bit

to the surface and can be further categorized as hydrostatic or stagnation pressures. The total pressure refers to the sum of forces caused by the transfer of momentum normal to a boundary. Shear forces refer to the tractive forces that act tangential to a boundary surface. In a general two dimensional problem, pressure and shear forces will both have x and y components. When considering forces applied by flow around an object, it is often convenient to resolve the forces acting in the downstream direction into a single drag force. Thus, the drag force is comprised of a surface drag due to tractive forces and a form drag due to pressure differentials. Similarly, the fluid forces acting perpendicular to the downstream direction are resolved into a single lift force. In the context of this biofilm model, the fluid forces acting on the biofilm structure in the x direction were resolved into a single drag force. The forces acting in the y direction were resolved into a single lift force.

Simulation Series

Series A, Maxwell Elastic Modulus Varied

Fluid-induced pressure and shear forces acted to deform the biofilm structure. In response to these applied loads, internal stresses developed in the biofilm. Moreover, the shape of the viscoelastic biofilm changed with time in response to the pressure and shear loads. In general, the fluid forces deformed the biofilms in the positive x and y directions. Thus, the biofilms were lifted and pushed downstream.

Not surprisingly, the x-component of the resultant of the shear and pressure forces, or collectively, the drag force, D, was positive throughout the deformation history of each simulation. This drag force deformed the biofilm in the downstream direction. Less predictable, however, was that D increased in magnitude as the cluster deformed despite the fact that the average bulk fluid velocity remained constant. The y-component of the resultant fluid force or lift force, L, tended to lift the biofilm, and in doing so, exposed the structure to the higher velocities and greater drag found in the upper parts of the flow field. However, lift forces did decrease as the biofilm cluster moved through deformation path. The combined effect was that pressure and shear reshaped the structure in such a way as to make it more susceptible to those same two forces. As Figure 2 illustrates, this initially hemispherical cluster deformed into a less streamlined geometry. The overall trend was such that the biofilm deformed into a less streamlined shape (i.e., subject to a greater drag force) but that the rate of this change decreased due to the influence of a decreasing lift force.

Though the Burger analog is not a simple elastic material, the Maxwell elastic modulus, G_1, can be regarded as a component of this biofilm's stiffness. More specifically, G_1 represents the biofilm's instantaneous elasticity. As such, lowering G_1 effectively softened the biofilm; increasing this coefficient made it less compliant. Drag forces increased as G_1 decreased. Conversely, lift forces decreased as G_1 decreased. The aforementioned progression of the biofilm hemisphere to a less streamlined shape was accelerated by decreasing G_1.

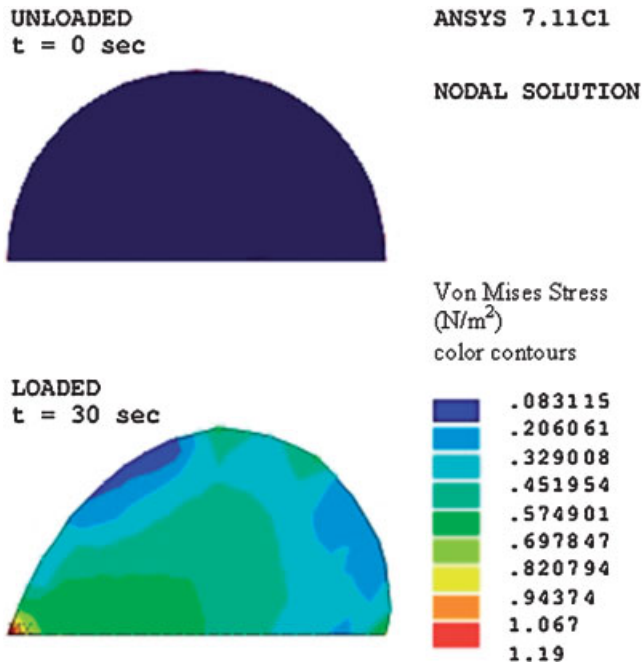

Figure 2. Stress distribution on cluster: Contours represent gradations of internal Von Mises stresses in N/m^2.

Interestingly, a significant change in the rate of increase in fluid forces was evident at approximately 5 s into the simulation (see Figs. 3 and 4). The stage from $t = 0$ s to $t = 5$ s was characterized by a rapid increase in the applied fluid forces. After $t = 5$ s the rate of change in lift and drag loads was much smaller. While the rate of change in lift and drag

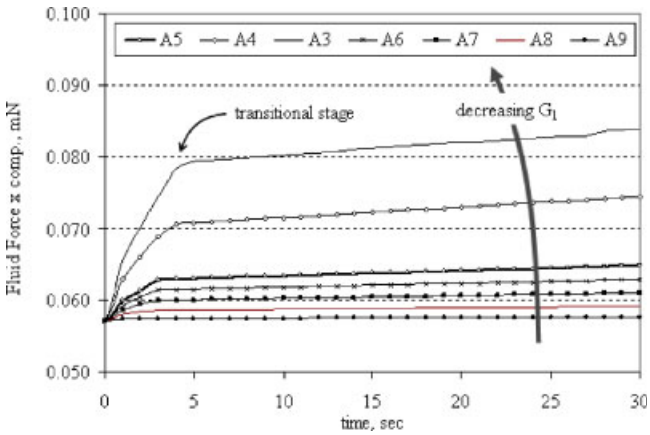

Figure 3. x component of the resultant fluid force versus G_1 for series A.

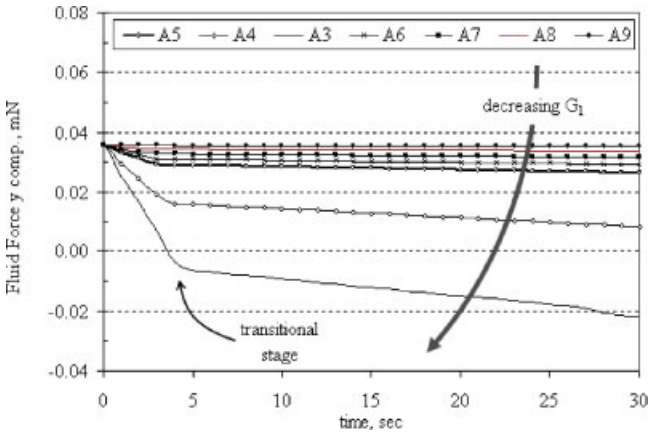

Figure 4. y component of the resultant fluid force versus G_1 for series A.

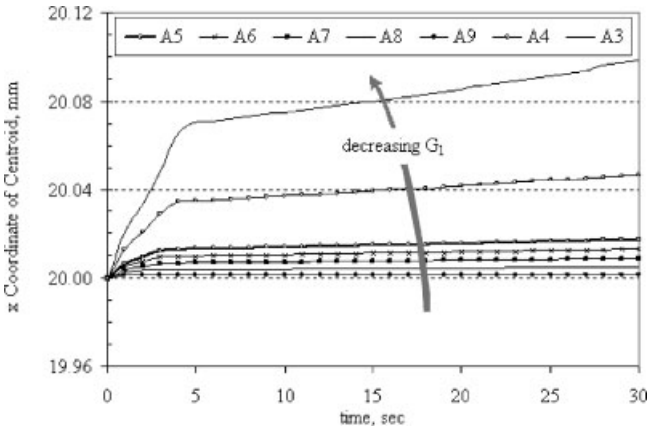

Figure 6. Changes in y centroid of biofilm cluster versus G_1 for series A.

varied with G_1, they were approximately constant during and after this transition stage for a fixed value of the Maxwell elastic coefficient. The changes in lift and drag were clearly a response to changes in biofilm shape. The change in shape is illustrated by the translation of the centroid of the structure (see Figs. 5 and 6).

Series B, Kelvin Elastic Modulus Varied

As with Series A, the shape of the viscoelastic biofilm changed with time in response to the pressure and shear forces. In general, displacements were not as great in Series B as they were in Series A. Again, the centroid of the structure was used as a measure of this change. The magnitudes of the displacement were not as great in this series as they were in Series A. A change of displacement rates was also evident in this set of simulations. In series B, these transitions to a new displacement rate occurred more quickly when compared to series A. Furthermore, this change occurred faster as the Kelvin elastic modulus, G_2, was decreased. However, the system approached a near steady state almost immediately after the transition stage. The ultimate displacement rate was relatively insensitive to G_2. Figures 7 and 8 show the change in the centroid's x and y coordinates with time.

Series C, Maxwell Elastic Modulus Varied

Again, fluid forces tended to both drag and lift the attached biofilm structure. While G_1 was varied in both Series A and C, the overall results of Series C more closely resembled those of Series B, not Series A. This suggests that the Maxwell viscous coefficient plays a dominant role in the ultimate displacement of the attached biofilm structure. Figure 9 shows the change in the resultant fluid force for each simulation in Series C.

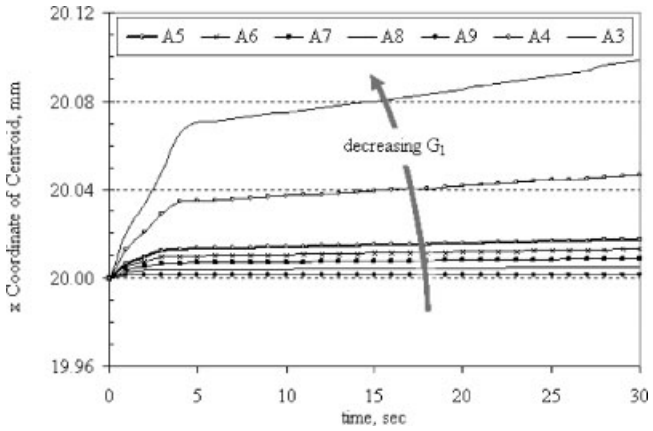

Figure 5. Changes in x centroid of biofilm cluster versus G_1 for series A.

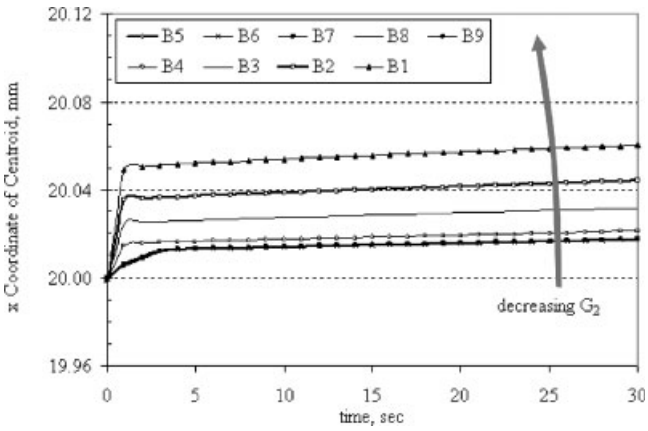

Figure 7. Changes in x centroid of biofilm cluster versus G_2 in series B.

DOI 10.1002/bit

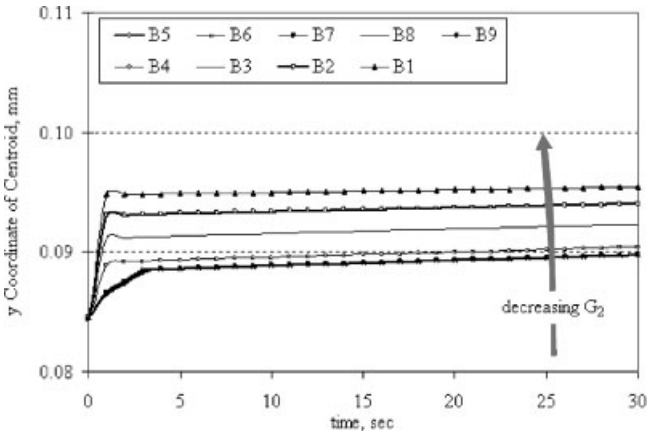

Figure 8. Changes in y centroid of biofilm cluster versus G_2 in series B.

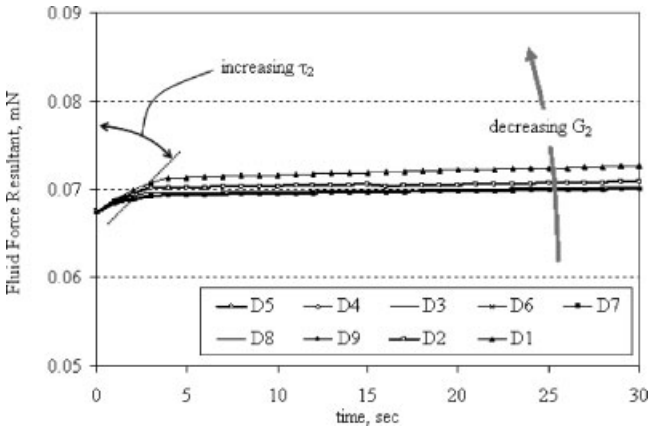

Figure 10. Changes in resultant versus G_2 in series D.

Series D, Kelvin Elastic Modulus Varied

As G_2 decreased, t_2 increased and this increase in the Kelvin relaxation time was expressed in the time required for the resultant fluid force (see Fig. 10) to reach a constant rate of increase.

Series E and F, Mean Channel Velocity Varied

A comparison of the channel velocity, V, to the resultant fluid forces provided insight into biofilm boundary layer penetration. In Series E, the ratio of channel velocity to the baseline velocity of Series A was 0.8. The initial ratio of resultant forces for the two series was 0.60. In all three simulations in Series E (E3, E5, E7) this force ratio decreased as the biofilm deformed over time (see Fig. 11). Softer biofilms (lower G_1) experienced a greater decrease in the force ratio. Conversely, when comparing the ratios of the resultants in Series F and Series A, it was found that the force ratio increased from 1.51 to 1.69 in the biofilm with the lowest Maxwell elastic modulus.

Series G and H, Biofilm Hemisphere Radius Varied

The nature of the results was similar to those in Series E and F. By increasing the radius, r, of the attached structure, the momentum transfer to the biofilm was increased. Figure 12 illustrates the effect of varying cluster size on the resultant fluid force impacting the biofilm.

Discussion

General trends in the interplay between cluster shape, hydrodynamic loads, and the material coefficients were evident. Many of these trends were observable precisely

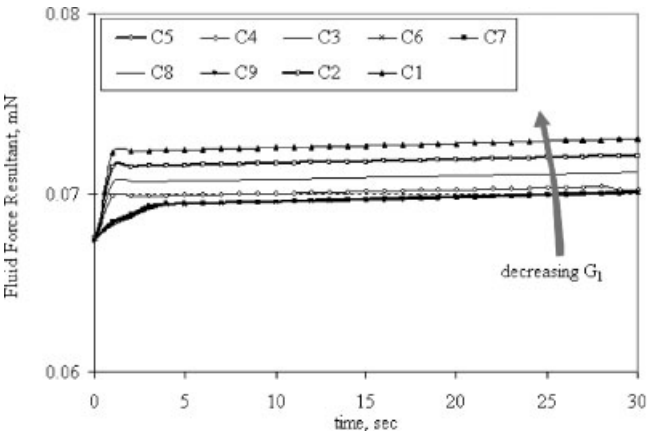

Figure 9. Changes in resultant versus G_1 in series C.

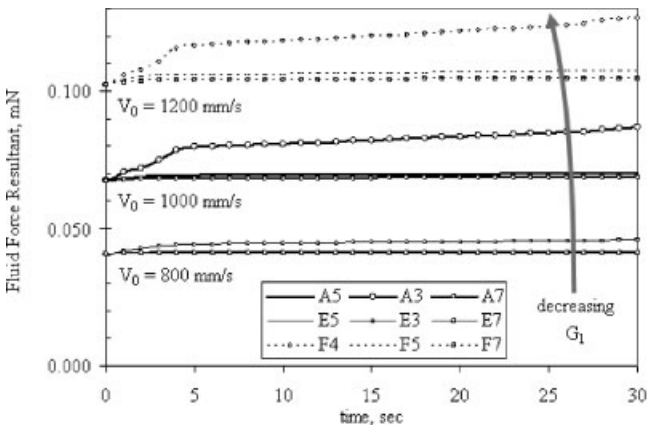

Figure 11. Changes in resultant versus G_1 for three different channel velocities; series A, E, and F.

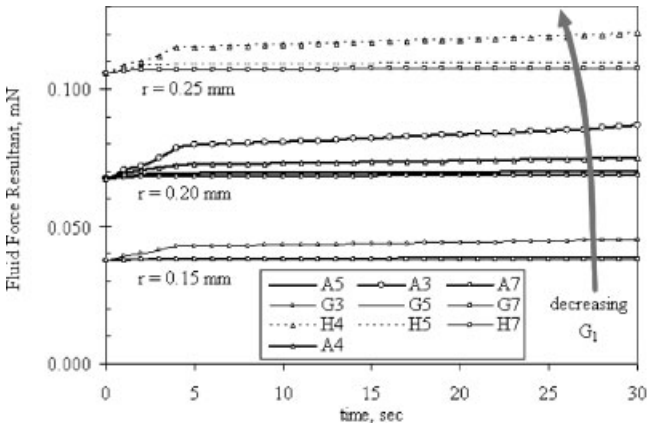

Figure 12. Changes in resultant versus G_1 for three different biofilm cluster radii; series A, G, and H.

because of the geometric simplicity of the biofilm cluster and because the boundary conditions, such as flow rate, pressure, and roughness, could be prescribed. These same parameters are not measurable in most laboratory experiments. The relevance of the viscoelastic relaxation time, the significance of flow rates on a compliant body and the potential value of dimensionless lift and drag coefficients are presented.

Relaxation Time and Removal Strategies

Relaxation times can be regarded as the time required for a viscoelastic material to dissipate internal stresses after being subjected to a constant strain instantaneously applied at $t = 0$ s. The Burger model possesses two different relaxation times, one for the Maxwell element and another for the Kelvin element. The Kelvin relaxation time for each simulation in series A was 5 s. This is approximately equal to the elapsed time between the start of the simulation and the change in slopes of the drag and lift forces versus time. Therefore, it is likely that the sharp changes in loading rates, best demonstrated in series A, were expressions of the relaxation time, τ_2, of the Kelvin element.

The behavior observed in series B agreed with the theoretical response of a Burger model which, at $t = \infty$, acts as a fluid (governed by the Maxwell dashpot). Recall that η_2 was held constant in series B thus explaining why the ultimate strain rates for all nine simulations were approximately equal. The changes in displacement rates of the centroid were also expressions of the Kelvin relaxation time and a metric of the time required to dissipate internal stresses in the biofilm. However, τ_2 was not distinguishable on the time axis of these plots. It was clear, however, that once the internal stresses in the biofilm were dissipated the resultant forces changed at approximately the same rate in each series B simulation. In short, the cluster responded as a viscoelastic fluid.

It is important to note that this expression of relaxation time was not merely an artifact of the numerical method or of the Burger material law. Indeed, these different modes of strain behavior have been observed in laboratory settings. It was noted anecdotally by Stoodley et al. (1999b) and measured by Towler et al. (2003). That the computational model reproduces this complex strain response underscores its accuracy.

Measurements of the relaxation time for a particular species may lead to improved biofilm removal strategies. Wholesale or partial detachment of a cluster would occur when the internal stresses exceed the material's failure stress. As outlined above, internal stresses in a biofilm governed by a linear viscoelastic material law are greatest prior to the expiration of the Kelvin relaxation time. At longer times, the biofilm has dissipated internal stress and flows as a fluid. Accordingly, the potential for removal by mechanically (i.e., hydrodynamically) loading the biofilm is greatest during the initial relaxation time. This would suggest that short duration, high velocity pulses in the flow field would prove more effective at inducing detachment than would sustained high flow events.

The Effect of High Flow Rates

As demonstrated in Figures 4 and 6, lift causes vertical deformation of the compliant biofilm. Vertical deformation creates a higher profile cluster. A higher profile structure is subject to larger velocities and, consequently, greater drag forces as illustrated in Figure 3. Real, turbulent flows do not have a uniform velocity distribution. The distribution is linear within the boundary layer and approximately logarithmic beyond the boundary layer. Therefore the effect of increasing load due to vertical deformation should be magnified in turbulent flows. In general, quantifying this effect is not possible because the boundary layer thickness is a function of Reynolds number and resultant forces were a function of the complete strain history. However, in general, the velocity increases as one moves away from the wall boundary. Thus, these simulations show that biofilm's capacity for deformation, as expressed by the material properties, is doubly important; lift creates a greater vertical profile for the fluid to impinge upon and drag forces vary non-linearly due to the non-uniform velocity distribution in turbulent flow.

The Effect of Lift and Drag on a Biofilm Cluster

Polar diagrams (see Appendix) were created using the results of Series A through Series H to investigate the relationship between drag and lift in a non-dimensional setting. Figure 13 is a polar diagram of the drag versus lift coefficients in Series A. All seven simulations started with the same initial drag and lift coefficients of 0.114 and 0.072,

DOI 10.1002/bit

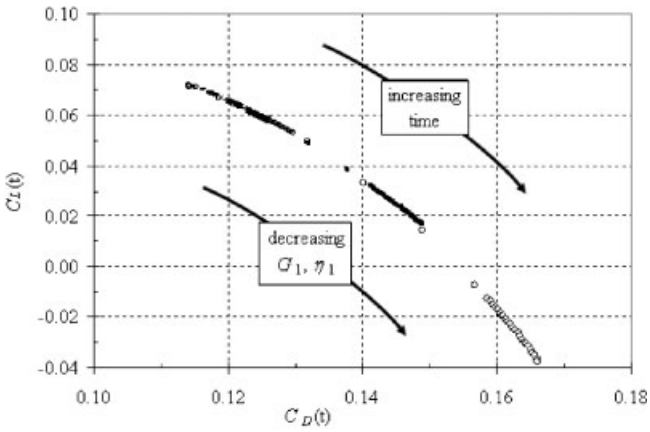

Figure 13. Polar diagram of lift versus drag on 0.20 mm biofilm cluster for Series A.

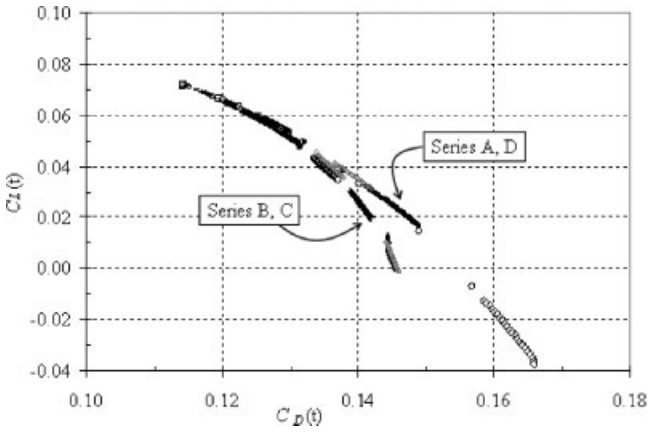

Figure 14. Composite polar diagram of lift versus drag on 0.20 mm biofilm cluster for Series A–D.

respectively. In each simulation, the biofilm hemispheres deformed in response to these forces and, consequently, this altered the forces that were applied later in time. As time advanced, the drag forces increased while the lift forces decreased. While the ultimate values of these coefficients differed among simulations, it is *very* interesting to note that the entire series plotted along the same curve. That is, the paths that each of these simulations took in reaching their final values of lift and drag were nearly identical. They differed only in how far along the path they progressed after 30 s. If the ratios of the lift and drag forces are indicators of deformed geometry, this also suggests that the deformation path was identical for each of these simulations.

In Series B, the Kelvin elastic modulus was varied while holding the Kelvin relaxation time constant. The coefficients of drag and lift for all nine simulations in this series were plotted on a polar diagram. The results indicated a pattern similar to the one seen in Figure 13. This tendency to preserve a common deformation history among a permutation set was also present in Series C and D. These behavior of these simulations are shown on Figure 14.

These polar diagrams demonstrate that varying a single elastic modulus in the Burger model, while holding either the viscous coefficient or the relaxation time constant, a similar deformation history is produced. The effect of varying the modulus is seen in how far into the deformation path (or how far down the path traced out on the polar diagrams) the simulation progress. Although each of these simulations produced a single deformation path and although each path originated at the same point, they did not produce the same path. When displayed on a common plot, a clear bifurcation in these curves was evident and is displayed in Figure 14. There was close agreement between Series A and D and between Series B and C. The previous examination of Series A and D demonstrated that these two series clearly expressed two different modes of behavior or rates of deformation. Furthermore, it was suggested that these different slopes were an expression of viscoelastic relaxation times. It seems likely therefore that the bifurcation of these polar paths in Figure 14 is also due to differences in relaxation times.

The effects of changing the mean channel velocity and the radius of the biofilm hemisphere were also examined using polar diagrams. Figure 15 is a polar diagram of the simulations in Series A, E, and F. Figure 16 is a similar plot demonstrating the effect of varying biofilm radius using Series A, F, and G.

As the mean channel velocity was increased from 800 to 1,000 mm/s to 1,200 mm/s the forces acting upon the attached biofilm increased. Figure 15 demonstrates a clear shift in the polar diagram as channel velocity is increased. Though more simulations may be required to determine the

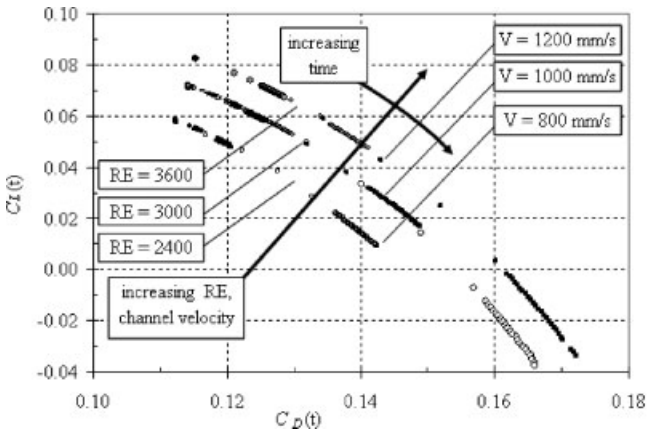

Figure 15. Polar diagram of lift versus drag on 0.20 mm biofilm cluster for Series A, E, and F.

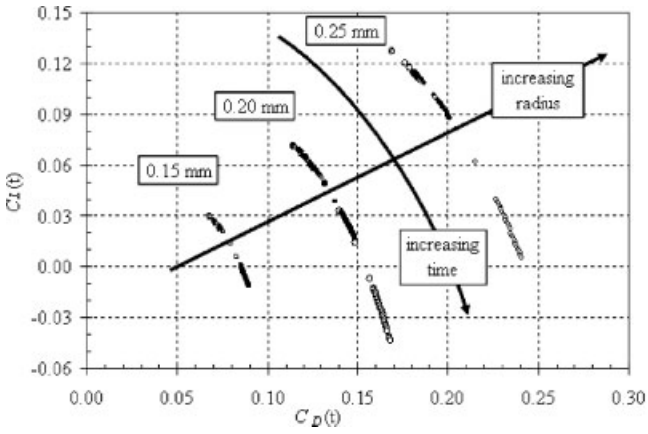

Figure 16. Polar diagram of lift versus drag on 0.15, 0.20, and 0.25 mm biofilm clusters for Series A, G, and H.

exact relationship, the shift does not appear to be proportional to the increase in velocity. The offset of the path taken at $RE = 3{,}600$ from the path taken at $RE = 3{,}000$ appears to be less than the similar offset from the path taken at $RE = 2{,}400$. Nevertheless, the separate paths are similar in character suggesting that a simple relationship may exist between channel velocity (and Reynolds number) and the polar diagram shift.

The radius of the biofilm structure was varied from 0.15 to 0.20 mm to 0.25 mm in Series A, F, and G. All other parameters were the same. A larger radius led to more biofilm surface area and a greater penetration of the viscous sub-boundary layer. The expectation was that the lift and drag forces acting on the larger biofilms would be greater. Figure 16 illustrates the increases biofilm size did indeed increase lift and drag forces. As with Figure 15, more simulations may be required to determine the actual relationship between radius and applied force. The offset for these paths do not appear directly proportional to the increase in radius. The offset from the path generated by a biofilm of radius 0.20 mm to the one with a radius of 0.25 mm is slightly greater than the offset to the path for a biofilm of radius 0.15 mm. It is likely that additional simulations may elucidate this relationship, however. Moreover, additional simulations examining the influence of other parameters may be equally insightful.

Conclusions

Biofilm is a ubiquitous natural phenomenon that impacts a variety of industrial applications. While some investigators have begun to study the structural behavior of microbial biofilms few have properly couched their observations in the context of a constitutive relation. A computational model was developed that solves the physics of fluid–structure interactions using the linear viscoelastic Burger constitutive relation. Simulations of hydrodynamically loaded biofilm structures were generated to illustrate the utility of the model and elucidate biofilm–fluid interaction.

All four of the independent Burger equation parameters were examined as well as the effects of mean channel flow velocity and biofilm size. It was shown that softer biofilms (characterized by lower elastic moduli) were highly susceptible to lift forces and consequently were subject to even greater drag forces found higher in the velocity field. Also, a bimodal deformation rate was observed in several simulation series. These two different rates of deformation were expressions of the two relaxation times in the Burger material law. This suggested that an attached cluster is most susceptible to detachment during the initial relaxation time. This result may prove useful in developing mechanical (hydrodynamic) removal strategies. Additionally, polar diagrams of lift versus drag suggested that the deformation paths taken by viscoelastic biofilms are largely insensitive to specific material coefficients. Softer biofilms merely follow the same path (as a stiffer biofilm) at a faster rate. These relationships may be useful in estimating the hydrodynamic forces acting on an attached biofilm based on changes in scale and cataloged material properties. Though additional refinement may be necessary, this model may help to develop a friction factor relationship for biofilm analogous to the Moody diagram for pipe flow. In light of the economic and human health impacts of interfacial biofilm growth and detachment, the value of these results is substantial.

Appendix

Polar Diagrams

In the study of airfoils, drag and lift coefficients are determined by normalizing the drag force by the velocity head. More specifically, the drag coefficient, C_D, is

$$C_D = \frac{F_D}{(\rho V^2/2)} \tag{13}$$

where F_D is the drag force, ρ is the density of the fluid, and V is the mean fluid velocity. The lift coefficient, C_L, is calculated in a similar manner and takes the form

$$C_L = \frac{F_L}{(\rho V^2/2)} \tag{14}$$

where F_L is the total lift force acting on the airfoil. By extending this argument to the study of the hydrodynamic impact on attached biofilms, one can use drag and lift coefficients as non-dimensional metrics of the forces on a biofilm structure. A polar diagram is a plot of the drag coefficient versus the lift coefficient (Vennard, 1940).

DOI 10.1002/bit

References

ANSYS. 2003. ANSYS theory Reference manual. Canonsburg, PA: ANSYS, Inc.

Bryers J, Characklis WG. 1981. Early fouling biofilm formation in a turbulent flow system: Overall kinetics. Water Res 15:483–491.

Callister WD. 1985. Materials Science and Engineering. New York, NY: John Wiley & Sons, Inc.

Characklis WG. 1979. Biofilm development and destruction, Final Report, EPRI CS-1554, Project RP902-1. Electric Power Research Institute, Palo Alto, CA, 1980.

Characklis WG. 1990. Microbial fouling. In: Characklis WG, Marshall KC, editors. Biofilms. New York, NY: John Wiley & Sons, Inc.

Currie IG. 1974. Fundamental mechanics of fluids. New York, NY: McGraw-Hill, Inc.

Debler WR. 1990. Fluid mechanics fundamentals. Englewood Cliffs, NJ: Prentice Hall.

Dockery J, Klapper I. 2001. Finger formation in biofilm layers. SIAM J Appl Math 62:853–869.

Findley WN, Lai JS, Onaran K. 1989. Creep and relaxation of nonlinear viscoelastic materials. Minneola, NY: Dover Publishing.

Flemming HC, Wingender J, Mayer C, Korstgens V, Borchard W. 2002. Cohesiveness in biofilm matrix polymers. SGM symposium 59.

Geesey G, Bryers J. 2000. Biofouling of engineered materials and systems. In: Bryers J, editor. Biofilms II: Process analysis and applications. New York: Wiley-Liss, Inc.

Giles RV, Evett JB, Liu C. 1956. Schaum's Outline of Theory and Problems of Fluid Mechanics and Hydraulics. New York, NY: McGraw-Hill, Inc.

Gjaltema A, Arts PAM, van Loosdrecht MCM, Kuenen JG, Heijnen JJ. 1994. Heterogeneity of biofilms in rotating annular reactors: Occurrence, structure and consequences. Biotechnol Bioeng 44:194–204.

Gujer W, Wanner O. 1990. Modeling mixed population biofilms. In: Characklis WG, Marshall KC, editors. Biofilms. New York, NY: John Wiley & Sons, Inc.

Hermanowicz WS. 1998. Two-dimensional simulations of biofilm development: Effects of external environmental conditions. In Conference proceedings, international specialty conference. Microbial ecology of biofilms: Concepts, tools and applications. Ed. Rittmann BE, Bishop P, Bouwer E, Cunningham A. Lake Bluff, IL.

Janna WS. 1993. Introduction to fluid mechanics, 3rd edition. Boston, MA: PWS Publishing Co.

Klapper I, Rupp CJ, Cargo R, Purevdorj B, Stoodley P. 2002. A viscoelastic fluid description of bacterial biofilm material properties. Biotechnol Bioeng 80:289–296.

Korstgens V, Flemming HC, Wingender J, Borchard W. 2001. Influence of calcium ions on the mechanical properties of a model biofilm of mucoid Pseudomonas aeruginosa. Water Sci Technol 43 49–57.

Mase GT, Mase GE. 1999. Continuum mechanics for engineers, 2nd edition. Boca Raton, FL: CRC Press LLC.

McCoy WF, Costerton JW. 1982. Fouling biofilm development in tubular flow systems. Dev Indus Microbiol 23:551–558.

Ohashi A, Harada H. 1994. Adhesion strength of biofilm developed in an attached-growth reactor. Wat Sci Tech 29:10–11, 281–288.

Patankar SV. 1980. Numerical heat transfer and fluid flow. Amsterdam: John Benjamins Publishing Co.

Picioreanu C, van Loosdretch MC, Heijnen JJ. 2001. Two-dimensional model of biofilm detachment caused by internal stress from liquid flow. Biotechnol Bioeng 72:205–218.

Picologlou BF, Zelver N, Characklis WG. 1980. Biofilm Growth and Hydraulic Performance. J Hydraul Div Am Soc Civ Eng 106(HY5): 733–746.

Rouse H. 1946. Elementary mechanics of fluids. New York, NY: John Wiley & Sons, Inc.; London, UK: Chapman & Hall, Limited.

Shackelford JF. 1985. Introduction to material science for engineers. New York, NY: Macmillan Publishing Company.

Stoodley P, Boyle JD, Dodds I, Lappin-Scott HM. 1997. Consensus model of biofilm structure. In: Wimpenny JWT, Handley PS, Gilbert P, Lappin-Scott HM, Jones M, editors. Biofilms: Community Interactions and Control. Cardiff: BioLine.

Stoodley P, Lewandowski Z, Boyle JD, Lappin-Scott HM. 1998. Oscillation characteristics of biofilm streamers in turbulent flowing water as related to drag and pressure drop. Biotechnol Bioeng 57:536–544.

Stoodley P, Lewandowski Z, Boyle JD, Lappin-Scott HM. 1999a. The formation of migratory ripple in a mixed species bacterial biofilm growing in turbulent flow. Environ Microbiol 1(5):447–455.

Stoodley P, Lewandowski Z, Boyle JD, Lappin-Scott HM. 1999b. Structural deformation of bacterial biofilms caused by short term fluctuations in flow velocity: An in-situ demonstration of biofilm viscoelasticity. Biotechnol Bioeng 65:83–92.

Stoodley P, Cargo R, Rupp CJ, Wilson S, Klapper I. 2002. Biofilm Material Properties as related to shear-induced deformation and detachment phenomena. J Ind Microb And Biotech 29:361–367.

Towler BW, Rupp CJ, Cunningham AB, Stoodley P. 2003. Viscoelastic Properties of a Mixed Culture Biofilm from Rheometer Creep Analysis. Biofouling 19:279–285.

Vennard JK. 1940. Elementary fluid mechanics. New York, NY: John Wiley & Sons, Inc.

Zelver N. 1979. Biofilm development and associated energy losses in water conduits. M.S. Thesis. Rice University. Houston, TX.